IEEE Photonics Journal
An IEEE Photonics Society Publication

Open Access

Pulse Response of an Ultracompact Grating-Based Monolithic Optical Compressor

Volume 10, Number 4, August 2018

C. Yang
E. Towe, *Fellow, IEEE*

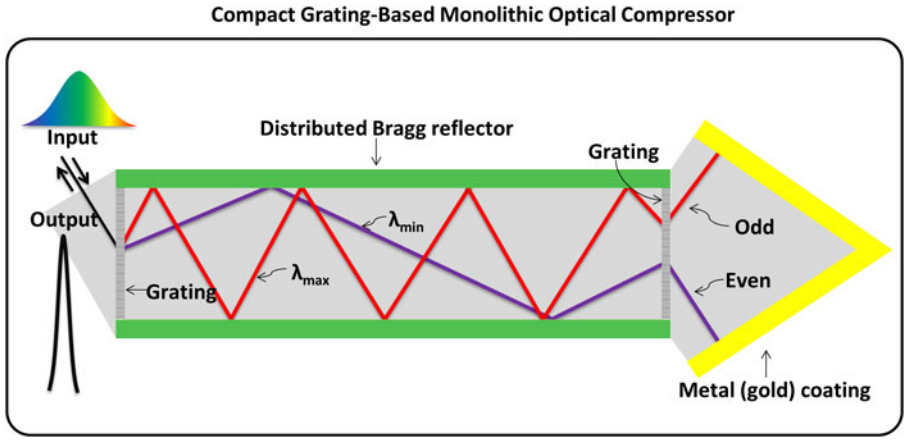

DOI: 10.1109/JPHOT.2018.2846557
1943-0655

IEEE photonics SOCIETY

IEEE

Pulse Response of an Ultracompact Grating-Based Monolithic Optical Compressor

C. Yang and E. Towe, *Fellow, IEEE*

Department of Electrical and Computer Engineering, Carnegie Mellon University, Pittsburgh, PA 15213 USA

DOI:10.1109/JPHOT.2018.2846557

Manuscript received May 23, 2018; accepted May 26, 2018. Date of publication June 27, 2018; date of current version July 10, 2018. This work was supported by the Defense Advanced Research Projects Agency under Grant HR0011-15-1-0009. Corresponding author: E. Towe (e-mail: towe@cmu.edu).

Abstract: The pulse response of a novel monolithic optical compressor is computationally simulated using the finite-difference time-domain method of electromagnetism. This compact and robust compressor can be made from a solid block of fused silica with all necessary optical components integrated into it. A beam folding mechanism implemented through use of integral Bragg reflectors serves to further reduce the volume of the device. The monolithic compressor is shown to successfully compress dispersion precompensated 0.6-ps Gaussian input pulses to output pulses with a duration of 25 fs.

Index Terms:

1. Introduction

Optical compressors used in high-power, chirped-pulse, laser amplification systems are usually large and cumbersome [1]–[3]. This makes their use outside of the laboratory, for example in industrial settings or in applications where flexibility, compact size, and portability is essential, very difficult or impossible. Numerous efforts have been expended in trying to reduce the size of the compressor [4]–[9]; none of these efforts have yet led to a robust configuration or a reduced overall compressor size. To provide a solution to some of the major challenges in existing compressors, we recently proposed a novel monolithic compressor that is both compact and robust [10]. By integrating the essential optical components, one can make a robust and monolithic compressor that requires no alignment. In the new scheme, folding the optical path with reflective coatings drastically reduces the compressor size; this is done by effectively reducing the longitudinal and transverse dimensions of the device. The new compressor is distinguished from the traditional one by its significantly reduced grating size—which has been a major limiting factor to portability and scaling in high-power handling capabilities of pulsed laser systems. In this work, we have developed a modeling and simulation scheme based on numerical solutions of the relevant Maxwell equations that govern the propagation of light pulses inside the new compressor; we use the finite-difference time-domain (FDTD) algorithm to numerically solve the equations. The initial temporally broad and chirped pulse input to the compressor is assumed to be Gaussian. At the output of the compressor, the compressed pulse is extracted and analyzed. The pulse is successfully compressed as predicted

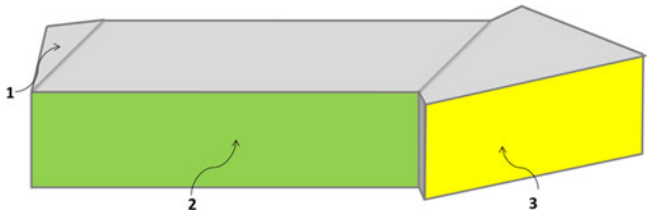

Fig. 1. Three dimensional illustration of a monolithic optical compressor.

by theory. The only aberration found is a small depression in pulse shape caused by a discontinuous change of the optical path length.

2. Structure and Operating Mechanism

Figure 1 is a geometrical illustration of the monolithic compressor. It is comprised of three conjoined solid and optically transparent blocks (labeled as 1, 2, 3) with an index of refraction that is larger than that of air. The medium in the regions represented in light grey color is fused silica; the green represents a distributed Bragg reflector that is formed at the edge of the fused silica, and the yellow color represents a low loss reflective coating (such as metallic gold). There are four surfaces on this device that are covered with reflective coatings: two on the front and rear surfaces of the central block labeled as 2, and two on the right-most block labeled as 3. Distributed Bragg reflectors are used instead of conventional reflecting coatings (which would otherwise be easier to form less expensively) because different wavelength components need to be reflected at the side surfaces of block 2 for a different number of times. The Bragg reflectors fold the beam, thus eliminating the need for a large transverse extent of block 2 for the spectral dispersion. Coatings on block 3, however, can be either distributed Brag reflectors or metal coatings. At the surfaces of block 3, all wavelength components are simply retro-reflected once.

Block 1 is a triangular prism. It is atomically welded to block 2 as shown in Fig. 1. The top and bottom surfaces of this block are right triangles; the remaining surfaces are rectangles of different sizes. The triangles subtend a 90-degree angle at one of the vertices not touching Block 2. For optimal performance, the input plane should be anti-reflection-coated. The role of this block is to balance the dispersion difference between air and the fused silica. The two opposite but parallel faces of Block 2 (on the left and right sides), have a grating written on them. Because of the high damage threshold requirement for gratings used in high-power laser systems, a transmission grating configuration should be used. Such gratings have damage thresholds that approach those of bulk materials [11]. In addition to the requirement for a high damage threshold for the grating coating, one should also determined the onset of any potential optical nonlinearity (by calculating the B-integral) prior to the fabrication of a compressor for high pulse energy applications. The third major component of the compressor, block 3, is an irregularly-shaped heptahedron. It is symmetric with respect to a vertical central plane in block 2. The two surfaces of block 3 that do not intersect with block 2 (shown in yellow in Fig. 2) serve the function of retro-reflecting incident beams back onto their original path; this means that one of these two surfaces is perpendicular to the incident beam direction, and the other is a mirror symmetry image of the incident beam direction with respect to an axial line in block 2. The two surfaces must therefore be covered with reflective coatings.

The manner in which light propagates through the composite monolithic compressor is shown in Fig. 2; this is an illustration from the top view of the structure. In operation, a train of temporally stretched pulses enter the compressor from the left-hand side as indicated; they impinge on the triangular prism in a direction that is almost perpendicular to the input surface, with a slight tilt to allow the separation of the input and output pulse trains. Inside block 1, all wavelength components travel along the same path. Upon transmission through the first diffraction grating, the beam is angularly spread by diffraction. The longest and shortest wavelength components follow the trajectories indicated with red and purple colored lines, respectively. When the light components strike the

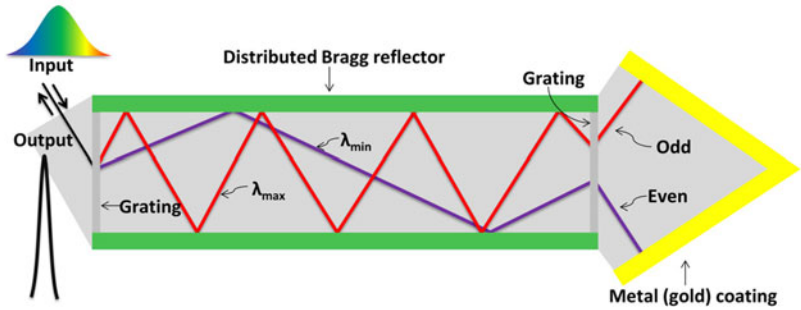

Fig. 2. Light trajectory inside a monolithic compressor structure. The first grating on the left spectrally disperses the light which then follows distinct paths according to wavelength until it hits the second grating on the left. Retro-reflection from block 3 forces the light to retrace its original path back to the output (input) where it is now compressed.

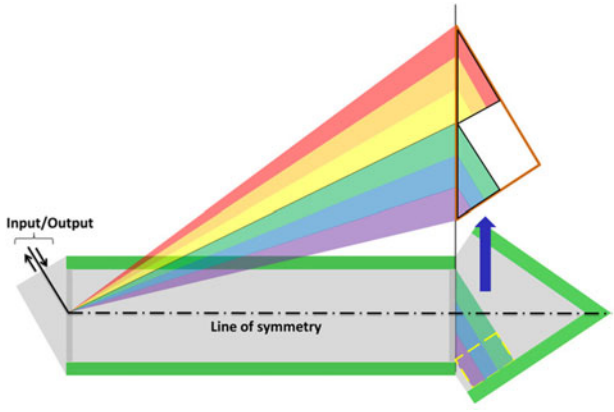

Fig. 3. Dispersive action within the monolithic compressor.

distributed Bragg reflectors on the sides of block 2, they are folded back into the block; different wavelength components may be reflected for a different number of times before they reach the second grating. These components may be separated into two groups: one set is reflected for an even number of times while the other is reflected for an odd number of times. The components that are folded for an even number of times in block 2 are deflected in a direction that is parallel to the original input beam after diffraction by the second grating; beam components folded by an odd number of times are diffracted at an angle that is a mirror symmetry of the incident beam with respect to the center line of block 2. The diffracted light components from the second grating (on the right) propagate through the body of block 3, and are retro-reflected by the coatings on the edges of block 3. Retro-reflection sends the components along the same path back to their original starting point in block 1. The returned composite beam is the output, with each pulse in the train of pulses temporally compressed to a much shorter width than the original input pulses. The theoretical calculation of how the beam folding mechanism implemented in the new compressor has already been thoroughly discussed in Ref [10]. Here, we will only be concerned with the determination of the response of the monolithic compressor to a single, chirped Gaussian pulse as input. A computational simulation based on the FDTD method [12]–[14] is carried out. Since there is nothing essential to the pulse compression process that is changing in the direction parallel to the grating ruling [15], a plane perpendicular to the grating ruling contains all the information needed for pulse analysis. This simplification allows one to use a two-dimensional FDTD simulation grid that works for a transverse-magnetic-polarized light.

Although block 3 of the compressor is a heptahedron, when viewed from the top (Fig. 3), it is a symmetric pentagon. Since the beam folding mechanism in the device does not alter the beam

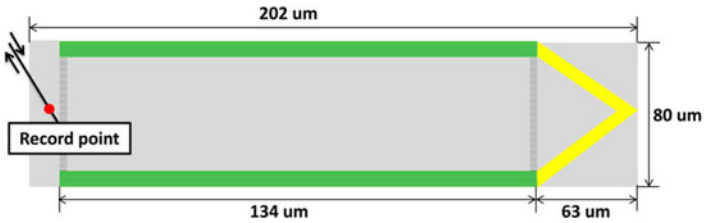

Fig. 4. Simulation domain for monolithic compressor.

physics, the rainbow-colored triangle in Fig. 3 correctly represents the beam dispersion in block 2 as it would in conventional compressors. If the beam spectrum is sub-divided into two bands, the portion of the spectrum for the lower band in block 3 is as shown in Fig. 3. Part of the lower spectrum enclosed in the yellow dashed square does not contribute to the optical path difference. This also happens for the upper band; the optical path additions in block 3 form a saw-tooth-like shape (shown in the upper right corner). The two grey surfaces of block 3 (see Fig. 3) serve no technical function. One then rightfully asks: why are these surfaces there? They are necessary for mechanical support purposes. Since block 3 is also made from bulk fused silica, it can be easily cut and polished to any desired shape before atomically welding it to block 2. Atomic welding of fused silica blocks as suggested here can be readily accomplished. The technology is well known [16]. For purposes of the computational simulations, there is no need to include the two side edges of block 1 because the relevant angles can be precisely and conveniently specified. A simplified structure shown in Fig. 4 is used to define the simulation domain of the monolithic compressor.

3. Simulation Setup and Results

We assume that the first block in the simulation grid is made of a rectangular fused silica material. Its shape does not change the manner in which the input pulse interacts with the compressor. As previously implied, block 2 and 3 are also solid fused silica, except for where the two gratings are written. The gratings are blazed to meet the Littrow condition. The red dot in Fig. 4 indicates the position where one records the optical electric field amplitude of the input and output pulses. It is generally known that the finite-difference time-domain algorithm is a powerful but computationally expensive simulation method. Although there is no intrinsic limit to how many field variables a software program based on the FDTD algorithm can handle, a large simulation grid is extremely slow and computationally costly in terms of time and memory usage. We have found that simulations with the same level of discretization but different grid sizes lead to the same pulse shapes. The only difference is the compression ratio. Thus, instead of simulating a full size monolithic compressor, with dimensions of several centimeters, a scaled-down version with dimensions in the hundreds of micrometers is constructed and simulated (Fig. 4). Although the input is based on light coming from a fiber system, the relevant compressor input/output parameters can be scaled for any dimensions to reflect pulse compression effects of different systems. The discretization level used for the present simulations is 30 points per wavelength. With a central laser operating wavelength set at 1030 nm, one spatial cell stands for 34.33 nm. The grating width is set at 80 μm, and the separation between the gratings is 134 μm. We use a grating constant of 600 nm.

A Gaussian pulse source is used for this simulation; the pulse is pre-compensated for the dispersion that is expected to occur in the compressor. In other words, the input pulse is manually chirped to have positive group velocity dispersion. At the beginning, the dispersion profile of the monolithic compressor system is not known. So the input pulse is assumed to have a linear positive chirp, as is usually the case when a pulse is stretched by propagating it through a standard single mode fiber. The relative (color coded) optical electric field amplitudes (in arbitrary units) inside the monolithic compressor can be plotted as shown in Fig. 5. Note that in this simulation experiment, the input Gaussian pulse is incident on the compressor at an angle of 59.13 degrees.

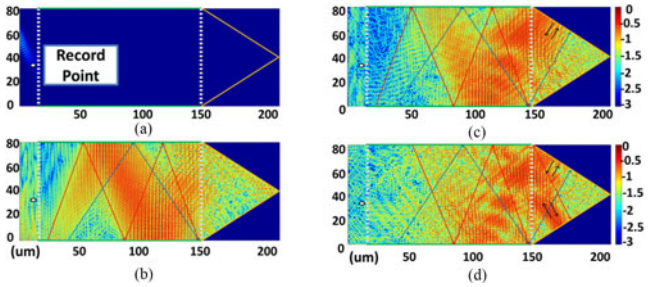

Fig. 5. Snapshots of simulated optical electric field amplitudes inside the monolithic compressor. (a) An input Gaussian pulse impinging on the grating. (b) Beam propagation profile inside the compressor before impinging on the second grating. (c) Lower spectral band of transmitted light through the second grating and its retro-reflected version. (d) Lower and upper spectral bands transmitted through the second grating and their retro-reflected versions. Logarithmic magnitude of the real electric field: 0 stands for 1, while 3 stands for 0.001.

Fig. 5(a) shows the oblique entrance of the chirped Gaussian input pulse into the compressor. The dashed lines represent the two integrated gratings of the monolithic compressor. The solid green lines at the top and bottom of the simulation grid indicate the distributed Bragg reflectors, while the orange lines on the right represent the metal retro-reflectors discussed earlier. The situation in Fig. 5(b) illustrates when the electric field has just arrived at the second grating on the right. Selected wavelength components are shown in red and blue, where the red represents the longest wavelength components and the blue represents the shortest wavelength components. Note that in this simulation, the compressor is designed to have a two-fold beam expansion in which the divergence of the diffracted beam at the second grating is twice as large as the width of the grating. This is the width of the simulation grid. As in the previous discussion, the diffracted beam can be sub-divided into two bands, with the lower band containing the shortest wavelength components, and the upper band containing the longest wavelength components of the pulse. The lower band components arrive at the second grating after reflection from the side distributed Bragg reflector at the bottom of block 2. This means the lower band impinges on the second grating at an oblique upward-going direction. The upper band, on the other hand, arrives at the second grating after reflection from the side distributed Bragg reflector at the top of block 2. This band impinges on the second grating at an oblique downward-going direction. The beam interactions at the second grating are shown in Fig. 5(c) and (d). Since the lower band of beam components travel for much shorter distances relative to the upper band components, they arrive at the second grating at an earlier time. The snapshot shown in Fig. 5(c) is for a case where the lower band has passed through the second grating while the upper band has not yet done so. In the snapshot in Fig. 5(d), the upper band of the beam has just passed through the second grating. It is diffracted in a direction that is parallel to the incident beam at the input. This beam is subsequently retro-reflected from block 3 to retrace its path back to the input.

The simulated optical electric field patterns show that the monolithic compressor structure interacts with the incident stretched pulse just as one would expect it to. Thus, an obliquely incident Gaussian pulse gets angularly spread out after diffraction by the first grating. The side Bragg reflectors then fold the diffracted beam back-and-forth within block 2 as it propagates toward the second grating. Different wavelength components are reflected for different number of times. The second grating re-collimates the spectral bands of the beam into parallel components. Although the two spectral bands travel in different directions, they are symmetric with respect to the center line of Block 2. As a consequence, the two spectral bands are retro-reflected by the reflectors on Block 3, which are perpendicular to the beam directions. As shown in Fig. 4, the input and output beams are monitored at the indicated red point. Arbitrary magnitudes of the input and output electric fields, along with their corresponding envelopes can be recorded at this point. We show in Fig. 6(a), the recorded linearly chirped input Gaussian pulse with its fully stretched temporal duration of 2 ps.

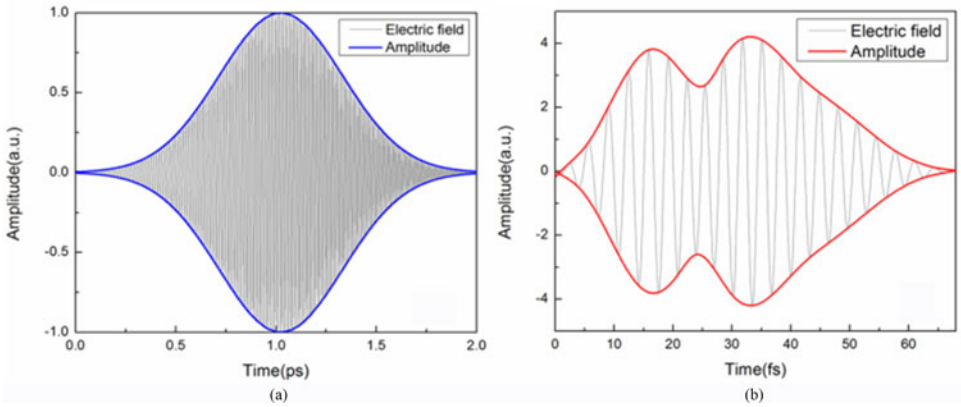

Fig. 6. Optical electric field amplitude of: (a) linearly chirped Gaussian pulse source; and (b) output pulse with depression in middle.

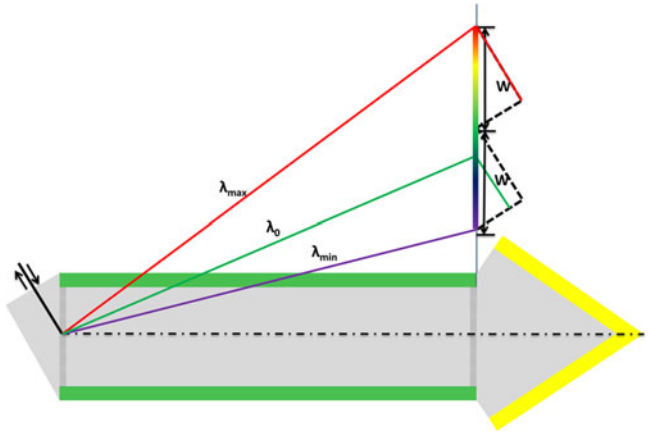

Fig. 7. Light path lengths inside compressor for selected wavelengths.

The full-width-at-half-maximum intensity is about 0.6 ps. Note that the input is normalized to unit maximum amplitude. The pulse envelop of the output as monitored at the exit point in Fig. 4 is shown in Fig. 6(b); although the envelope is still Gaussian, there is a slight depression near the middle. However, there is no chirp in the pattern inside the pulse envelop, clearly showing that the instantaneous frequency is constant. This is an indication that the pulse has been successfully compressed close to its shortest duration of about 25 fs.

We now return to explain the observation of the depression in the output pulse envelop. Its existence can be understood by re-examining the structure of the monolithic compressor shown in Fig. 7; included in this illustration are traces of selected wavelength components of the input pulse. The solid black line represents the input/output beam. The two dashed triangles represent the additive optical paths after a pulse exits the second grating; each path (for the selected wavelength components), has a length equal to the grating width W. Note that the red lines represent the beam paths for the longest wavelength component, while the green represents the central wavelength, and purple stands for the shortest wavelength. As noted earlier, the optical path lengths for all wavelength components are not continuous after the second grating. There is a discontinuity in the beam divergence; this happens at the point where the two dashed triangles (with the saw tooth features) touch (see Fig. 7). Because of this, one expects the compressed pulse to be split. The split is responsible for the depression in the output pulse envelop in Fig. 6(b). We note that the lower spectral band, which contains the shortest wavelength components, appears to have more

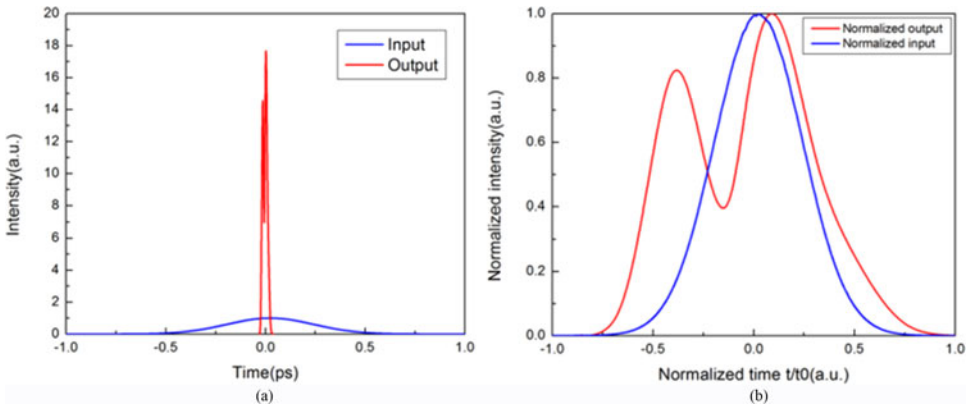

Fig. 8. Field intensity profiles for the (a) input and output pulses; and (b) corresponding normalized intensities for the input and output.

wavelength components. This is easily understood as a consequence of the fact that a grating spatially spreads out longer wavelengths much more than it does shorter wavelengths. According to the grating equation, the central wavelength of the pulse is diffracted at an angle that is closer to the shortest wavelength than to the longest one; the central wavelength is labeled as $\lambda 0$ in Fig. 7. This analysis therefore indicates that the lower spectral band contains more wavelengths than the upper band.

We show the input and output field intensities for the pulses recorded at the monitoring point in Fig. 8(a). Notice how the output pulse (in red) is temporally compressed to a much narrower width than the (blue) input pulse. Since it is difficult to discern the pulse details as extracted from the raw data, we show the normalized intensity plots in Fig. 8(b). Despite the depression in the output pulse shape, it is still clearly Gaussian. The origin of the depression has already been explained.

4. Conclusions

Now that the response of the new compact compressor to linearly chirped input Gaussian pulses is known, one can design a matching nonlinearly chirped fiber Bragg grating to use with the compressor. It is generally straightforward to devise a dispersion profile of a fiber Bragg grating structure to any desired profile. Knowledge of the calculated (simulated) pulse response of the compressor allows one to create a fiber Bragg grating structure that incorporates the “opposite” of the saw-tooth-like optical path length feature in the compressor so that the effect is canceled out in the final output pulse shapes, leading to clean, ultra-short and high-peak-power laser pulses.

In summary, we have successfully modeled and computationally simulated the function of a monolithic ultra-compact, grating-based compressor. The simulations show that the new compressor operates as expected.

Acknowledgment

The authors gratefully acknowledge use of facilities in the Optics and Photonics Laboratory at Carnegie Mellon University.

References

[1] T. Eidam *et al.*, *Opt. Lett.*, vol. 35, p. 94, 2010.
[2] D. J. Richardson, J. Nilsson, and W. A. Clarkson, *J. Opt. Soc. Amer. B*, vol. 27, p. 63, 2010.
[3] J. Limpert *et al.*, *Opt. Lett.*, vol. 28, p. 1984, 2003.
[4] A. Galvanauskas, M. E. Fermann, and D. Harter, *Appl. Phys. Lett.*, vol. 66, p. 1053, 1995.
[5] J. H. Sung, J. Y. Park, T. Imran, Y. S. Lee, and C. H. Nam, *Appl. Phys. B*, vol. 82, p. 5, 2006.

[6] J. Park, J. Lee, and C. Nam, *Opt. Lett.*, vol. 34, p. 2342, 2009.
[7] A. Braun, C. Horvath, and X. Liu, U.S. Patent No. 6 081 543, Jun. 27, 2000.
[8] M. Y. Shverdin *et al.*, *Opt. Lett.*, vol. 35, p. 2478, 2010.
[9] M. Lai, S. T. Lai, and C. Swinger, *Appl. Opt.*, vol. 33, p. 6985, 1994.
[10] C. Yang and E. Towe, *J. Opt. Soc. Amer. B*, vol. 33, p. 2135, 2016.
[11] T. Clausnitzer *et al.*, *Appl. Opt.*, vol. 42, p. 6934, 2003.
[12] K. S. Yee, *IEEE Trans. Antennas Propag.*, vol. 14, p. 302, 1966.
[13] A. Taflove and C. Susan, *Computational Electrodynamics*. Norwood, MA, USA: Artech House, 2005.
[14] J. B. Schneider, "Lecture materials for EE 535," ch. 3, Washington State Univ., Pullman, WA, USA, 2007.
[15] O. E. Martinez, *Quantum Electron.*, vol. 23, p. 59, 1987.
[16] M. M. R. Howlader, S. Suehara, and T. Suga, *Sens. Actuators A*, vol. 127, p. 31, 2006.